Low energy antiproton-nucleus elastic scattering

V. Ashford,* M. E. Sainio, M. Sakitt, and J. Skelly
Brookhaven National Laboratory, Upton, New York 11973

R. Debbe, W. Fickinger, R. Marino, and D. K. Robinson
Case Western Reserve University, Cleveland, Ohio 44106

(Received 13 April 1984)

We have studied antiproton elastic scattering on Al, Cu, and Pb for two incident momenta: 514 and 633 MeV/c. The angular region covered extends from the forward Coulomb region to approximately 30 deg. The differential cross sections were analyzed using a nonrelativistic optical potential of the Woods-Saxon form, with the imaginary shape taken from electron scattering data. We obtained fits for the strengths of the real and imaginary parts of the potential, (V_0, W_0), of (51, 116) MeV for Al, (12, 71) MeV for Cu, and (12, 278) MeV for Pb.

The scattering of antiprotons by nuclei is an interesting area of research, both theoretical and experimental. In contrast to some progress in the theory,[1] experimental data in the low energy region are just beginning to become available.[2–4] We present here the results of a systematic study of antiproton scattering by three different nuclei: aluminum, copper, and lead.

Data for this experiment were acquired in conjunction with an experiment on antiproton-proton interactions using the Low Energy Separated Beam line (C4) at the Brookhaven Alternating Gradient Synchrotron (AGS). The C4 beam was tuned to provide antiprotons of momenta 514 and 633 MeV/c at the metal target. At these energies, the beam provides on the order of 1000 antiprotons per pulse.

The principal components of the experimental setup are indicated in Fig. 1. The beam was partially separated and tagged electronically with a series of counters (S1 and S3). These time-of-flight counters and several dE/dx counters were used to select the incoming antiprotons. In addition, a lucite Čerenkov counter ($\check{C}$) was used as a pion veto. This resulted in a tagged antiproton beam with better than 99% purity. The only trigger requirement was an incoming antiproton. The beam was monitored by a series of counters (S4) placed much further downstream. For each trigger, all electronic data were read out and recorded on magnetic tape.

The incoming beam track was measured in a series of four triplet drift chambers (DC1–12), each triplet consisting of an x, u, and v, plane. The coordinates of the outgoing scattered particle were measured by a series of 18 doublet drift chambers (DC13–30), six each for x, u, and v. Each plane covered an area of approximately 1 m^2. The resolution of the chambers was about 300 μm. The final angular resolution is therefore completely dominated by multiple scattering in the target.

The scattered particle also passed through one of two hodoscopes, H1 and H2 in Fig. 1. The first hodoscope H1 had a square hole at its center to allow passage of the forward scattered particles to the downstream drift chambers and H2. The H2 hodoscope consisted of two orthogonal

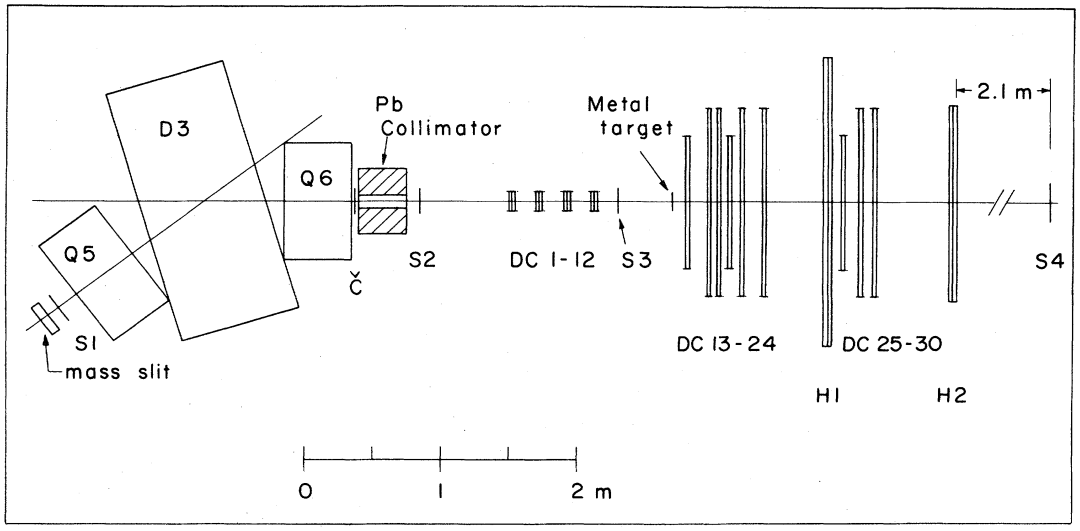

FIG. 1. Layout of the antiproton scattering experiment in the C4 low energy separated beam at the Brookhaven AGS.

sets of rectangular elements 5.1 or 10.2 cm wide and 101.6 cm long. The H1 elements were 10.2 cm wide by 152.4 cm long. Each element had a photomultiplier at each end of the scintillator (except those adjacent to the hole in H1). The times of flight and pulse heights for all counters were recorded. A minimum of three photomultipliers was required to distinguish between outgoing pions from annihilations and antiprotons. The efficiency for tagging an outgoing antiproton after scattering was about 95% per plane. The geometric acceptance was essentially 100% out to about 30 deg in the laboratory.

The aluminum, copper, and lead targets had natural isotopic composition. Each run was done with two different target thicknesses in order better to understand the resolution and secondary scattering.

In our analysis of the data, events in which the secondary track hit the downstream counters (S4) and had a time of flight corresponding to antiprotons were not reconstructed since they are within the multiple scattering region. A subsample of these events was completely reconstructed to correct for the effects of this cut on the forward scattering.

The pattern recognition program separately reconstructs tracks from the beam chambers and the downstream chambers. For both the beam and the secondary track we required a minimum of three points in two coordinates and at least two hits in the third coordinate. The secondary reconstruction efficiency clearly depends on angle, due both to the intrinsic performance of the drift chambers and to the fact that wide angle scatters intersect only the first two thirds of the downstream drift chamber planes. The angular dependence of the efficiency was determined by use of the hodoscopes. By identifying a sample of antiprotons from time of flight and pulse height in the H1 and H2 hodoscopes and comparing with pattern recognition results, we mapped this efficiency as a function of angle. The resulting efficiency varies from approximately 97% in the forward direction to 65% in the 20 to 30 deg region with a mean efficiency about 95%.

For the determination of the cross sections, we selected events in which the incident antiproton was successfully reconstructed and intersected a 10 by 10 cm^2 at the plane of the 15 by 15 cm metal target.

We required that the outgoing track appear in the appropriate hodoscopes and give a time of flight and pulse height consistent with that expected for an antiproton. Figure 2 shows scatter plots of pulse height versus time of flight for three individual hodoscope elements corresponding to scattering angles of about 8, 13, and 18 deg. The times of flight are the averages of the values from opposite ends of the hodoscope elements. Note that the numbers of pions and antiprotons are about equal at the widest angle. The antiproton and pion regions are clear in all three plots even in a single hodoscope element. The simultaneous requirements that two hodoscope planes register both time of flight and pulse height in selected antiproton zones result in excellent separation of the pions and antiprotons, with less than 5% contamination of either sample by the other at all angles.

The final numbers of events were corrected for the effects of all the inefficiencies and the cuts made on the data. The uncertainty in these corrections is significantly less than our statistical errors.

The target thicknesses were (0.229, 0.686 cm) for aluminum, (0.099, 0.284 cm) for copper, and (0.081, 0.244 cm) for lead. The differential cross sections determined from the two thicknesses were in agreement with one another at angles greater than three times the mean multiple scattering angle expected for the thick target. We therefore merged the thick and thin target data in that region and used the

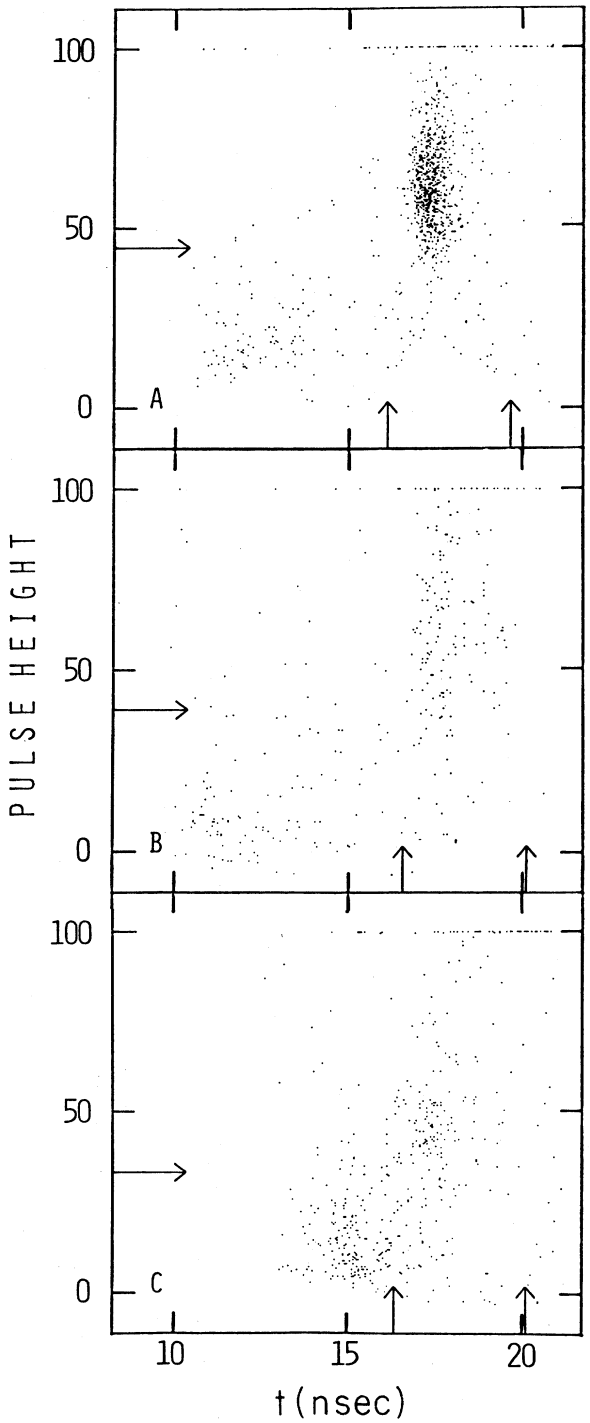

FIG. 2. Scatter plots of the time of flight vs the pulse height in the scintillator hodoscopes. Parts A, B, and C are for individual scintillator elements at scattering angles 8, 13, and 18 deg, respectively. The arrows indicate the borders of the selected antiproton zones. Antiprotons must satisfy such criteria in two hodoscope planes.

thin target data alone in the forward region. The optical model fits, which are described in the following section, take into account the effects of multiple scattering on the angular resolutions.

It is important to note that we do not measure the momentum of the outgoing scattered particle. Therefore, while the track is identified as an antiproton, it might have lost energy due to nuclear excitations. Our results are therefore quasielastic cross sections, which include low lying nuclear excitations.

Our final results for $d\sigma/d\Omega$ for the three targets and two momenta are shown in Fig. 3. We analyze the elastic cross sections in terms of a nonrelativistic optical potential model.

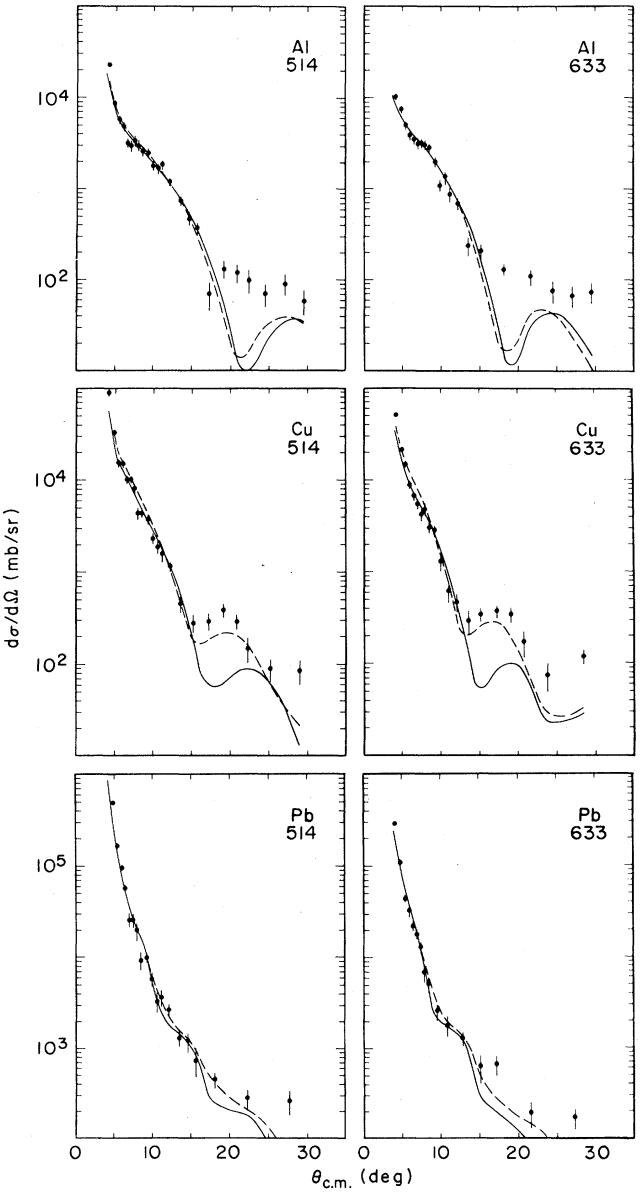

FIG. 3. The measured differential cross sections for antiprotons scattered by nuclei for the two energies and three metals indicated. The two sets of curves correspond to optical model fits and are described in the text. Solid curves refer to solutions *A*; dashed curves refer to solutions *B*.

The potential is taken in the form

$$V_{\rm opt}(r) = -V_0 f_R(r) - iW_0 f_I(r) \ , \tag{1}$$

where f_R and f_I have the Woods-Saxon shape

$$f_{R,I}(r) = \left[1+\exp\left(\frac{r-R_{R,I}}{a_{R,I}}\right)\right]^{-1} \ . \tag{2}$$

We are guided by the folding model, in which the optical potential is developed by folding the nuclear density determined from electron scattering experiments[5] with an effective $N\bar{N}$ potential.

We have used the program A-THREE[6] to fit the data to the potential in Eq. (1). Separate fits were made for each metal; each material was assumed to consist of a single isotope. The data from the two energies were fitted simultaneously. In all fits, we have searched for the best values of the depth parameters: V_0 which is related to the elastic part of the amplitude, and W_0 which is related to the annihilation or absorptive part.

There has been some discussion[7,8] concerning the choice of the geometric parameters: the R's, which scale the range of the interaction, and the a's, which describe the diffusivity, or the rate at which the interaction drops off. Therefore, we have tried fits with various geometries, in which these parameters are allowed to vary, or are fixed to values determined by electron scattering experiments, or ranges fixed at values proportional to $A^{1/3}$.

Since we cannot distinguish between pure elastic scattering and nuclear excitations, but expect that in the forward angular region the pure elastic scattering will be dominant, we first restrict our fitting to that region which should be described by the model. Good fits to the data at angles smaller than the diffraction minima (up to about 15 deg) are obtained for values of V_0 in the range 10–50 MeV and values of W_0 in the range 50–300 MeV. Both parts of the potential are attractive. These values are comparable to those measured in carbon, aluminum, and copper by Nakamura *et al.*[3]

In one of our sets of fits (solutions *A*), which have χ^2-values ranging from 1.0–1.8 per deg of freedom, we have fixed the absorptive radius and diffusivity to the electron scattering values,[5] since the short range annihilation interaction might be expected to track the nuclear charge distribution.[7] In addition, following Ref. 8, we set R_R equal to R_I, so that a_R is the only adjustable geometric parameter. We show in Table I the results of these fits. While a_R for copper is considerably larger than that for aluminum and lead, the fit is not very sensitive to a_R. The fitted differential cross sections are shown by the solid curves in Fig. 3.

Solutions *A*, obtained by fitting the forward region do not reproduce the large angle region, suggesting the presence of nuclear excitations in that region. In addition, attempts to fit the entire region with solution *A* geometry do not lead to any successful fits. We have also compared the data to a commonly used geometry[3,7] in which we fix $a_R = a_I = 0.52$ fm, $R_R = 1.3A^{1/3}$ fm, and $R_I = 1.1A^{1/3}$ fm. These sets of fits (solutions *B*) over the entire angle region, yield χ^2 values of the order of 2–4 per deg of freedom. These solutions are shown in Fig. 3 as the dashed lines. The parameters (V_0, W_0) are (22, 100) MeV for Al, (40, 140) MeV for Cu, and (33, 224) MeV for Pb. Because these fits include the region where nuclear excitations could be significant, we do not expect, *a priori*, good agreement. For both sets of

TABLE I. Results of the optical model solutions *A*.

	V_0 (MeV)	W_0 (MeV)	a_R (fm)	R_R (fm) = R_I (fm) fixed	a_I (fm) fixed
^{27}Al	51	116	0.56	3.07	0.52
^{63}Cu	12	71	0.90	4.21	0.59
^{208}Pb	12	278	0.55	6.62	0.55

solutions (*A* and *B*) we assign an uncertainty of ±15 MeV for V_0 and W_0.

We see an excess of events in the large angle region over the optical model predictions for pure elastic scattering. Our contamination in the region by annihilation pions is less than 5%. We therefore conclude that the wide angle data include nuclear excitation events. Such effects have been clearly seen at LEAR in antiproton scattering by carbon, in which the minimum was essentially filled in by antiprotons associated with a well defined (2^+, 4.4 MeV) excited state in carbon.[4]

We conclude that the optical model satisfactorily describes our data in the forward region in a momentum independent manner. While both geometries, solutions *A* and solutions *B*, yield reasonable fits in the forward direction, with solution *A* giving somewhat lower χ^2, we prefer solutions *A* because it is based on electron scattering data.

We would like to thank S. Kahana for helpful discussions and encouragement during the course of this experiment. We would like to acknowledge the excellent technical assistance provided by the staff of the Accelerator Department at Brookhaven National Laboratory. This work was supported by the U.S. Department of Energy under Contract No. DE-AC02-76CH00016 and by the National Science Foundation under Contract No. PHY80-20418.

*Present address: Stanford Linear Accelerator Center, Stanford, California.

[1]S. Kahana, in *Workshop on Physics at LEAR, Erice, 1982,* edited by U. Gastaldi and R. Klapisch (Plenum, New York, 1984), p. 495.

[2]D. Garreta, in *Workshop on Physics at LEAR, Erice, 1982,* edited by U. Gastaldi and R. Klapisch (Plenum, New York, 1984), p. 533. J.-C. Peng, in Proceedings of the Third Los Alamos Meson Physics Facility II Workshop, Los Alamos, 1983, edited by John C. Allred *et al.*, Report No. LA-9933-C, 1983, p. 531.

[3]K. Nakamura *et al.*, Phys. Rev. Lett. **52**, 731 (1984).

[4]D. Garreta *et al.*, Phys. Lett. **135B**, 266 (1984).

[5]C. W. DeJager, H. DeVries, and C. DeVries, At. Data Nucl. Data Tables **14**, 497 (1974).

[6]E. H. Auerbach, Comput. Phys. Commun. **15**, 165 (1978).

[7]E. H. Auerbach, C. B. Dover, and S. H. Kahana, Phys. Rev. Lett. **46**, 702 (1981).

[8]J. A. Niskanen and A. M. Green, Nucl. Phys. **A404**, 495 (1983).